

Research Articles: Behavioral/Cognitive

Intrinsic neural timescales in the temporal lobe support an auditory processing hierarchy

<https://doi.org/10.1523/JNEUROSCI.1941-22.2023>

Cite as: J. Neurosci 2023; 10.1523/JNEUROSCI.1941-22.2023

Received: 25 October 2022

Revised: 21 February 2023

Accepted: 2 March 2023

This Early Release article has been peer-reviewed and accepted, but has not been through the composition and copyediting processes. The final version may differ slightly in style or formatting and will contain links to any extended data.

Alerts: Sign up at www.jneurosci.org/alerts to receive customized email alerts when the fully formatted version of this article is published.

Intrinsic neural timescales in the temporal lobe support an auditory processing hierarchy

Abbreviated title: Timescales hierarchy supports auditory processing

Riccardo Cusinato^{1,2,*}, Sigurd L. Alnes^{1,2,*}, Ellen van Maren², Ida Boccalaro², Debora Ledergerber³, Antoine Adamantidis², Lukas L. Imbach³, Kaspar Schindler², Maxime O. Baud², Athina Tzovara^{1,2,4,#}

1 Institute of Computer Science, University of Bern, Switzerland;

2 Center for Experimental Neurology - Sleep Wake Epilepsy Center - NeuroTec, Department of Neurology, Inselspital, Bern University Hospital, University of Bern, Switzerland;

3 Swiss Epilepsy Center, Klinik Lengg, Zurich, Switzerland;

4 Helen Wills Neuroscience Institute, University of California Berkeley, USA

** These authors contributed equally to this work*

Corresponding author: athina.tz@gmail.com

Acknowledgments

This work is supported by the Inselspital University Hospital Bern, the Interfaculty Research Cooperation “Decoding Sleep: From Neurons to Health & Mind” of the University of Bern (AA, IB, AT, SLA), the Swiss National Science Foundation (AA, #320030_188737 AT), the European Research Council (CoG-725850 to A.A.), the Synapsis Foundation (AA), the University of Bern (AA), and the Fondation Pierre Mercier pour la science (AT). The authors thank Prof. Johannes Sarnthein for support with recordings and feedback on the manuscript.

Conflict of interests

MOB holds shares with Epios SA, a medical device company based in Geneva.

Number of pages: 42

Number of figures: 5, tables: 5

Number of words: Abstract: 168, Introduction: 617, Discussion: 1477

1 Abstract

2 During rest, intrinsic neural dynamics manifest at multiple timescales, which progressively
3 increase along visual and somatosensory hierarchies. Theoretically, intrinsic timescales are
4 thought to facilitate processing of external stimuli at multiple stages. However, direct links
5 between timescales at rest and sensory processing, as well as translation to the auditory
6 system are lacking. Here, we measured intracranial electroencephalography in 11 human
7 patients with epilepsy (4 women), while listening to pure tones. We show that in the auditory
8 network, intrinsic neural timescales progressively increase, while the spectral exponent flattens,
9 from temporal to entorhinal cortex, hippocampus, and amygdala. Within the neocortex, intrinsic
10 timescales exhibit spatial gradients that follow the temporal lobe anatomy. Crucially, intrinsic
11 timescales at baseline can explain the latency of auditory responses: as intrinsic timescales
12 increase, so do the single-electrode response onset and peak latencies. Our results suggest
13 that the human auditory network exhibits a repertoire of intrinsic neural dynamics, which
14 manifest in cortical gradients with millimeter resolution and may provide a variety of temporal
15 windows to support auditory processing.

16 Significance statement

17 Endogenous neural dynamics are often characterized by their intrinsic timescales. These are
18 thought to facilitate processing of external stimuli. However, a direct link between intrinsic timing
19 at rest and sensory processing is missing. Here, with intracranial electroencephalography
20 (iEEG), we show that intrinsic timescales progressively increase from temporal to entorhinal
21 cortex, hippocampus, and amygdala. Intrinsic timescales at baseline can explain the variability
22 in the timing of iEEG responses to sounds: cortical electrodes with fast timescales also show

23 fast and short-lasting responses to auditory stimuli, which progressively increase in the
24 hippocampus and amygdala. Our results suggest that a hierarchy of neural dynamics in the
25 temporal lobe manifests across cortical and limbic structures and can explain the temporal
26 richness of auditory responses.

27

28 Introduction

29 The human brain gives rise to rich neural dynamics, which play a fundamental role in
30 processing sensory information. Intrinsic dynamics of the brain operate at multiple timescales
31 (Hasson et al., 2008; Honey et al., 2012; Murray et al., 2014; Raut et al., 2020) through
32 oscillatory (Frauscher et al., 2018; Mahjoory et al., 2020; Vezoli et al., 2021) and non-oscillatory
33 (Gao et al., 2020) processes. In the visual and somatosensory systems, intrinsic timescales
34 manifest at rest, in ongoing neural activity: primary areas exhibit short timescales that may
35 facilitate a quick reaction to incoming stimuli (Murray et al., 2014; Siegle et al., 2021). These
36 progressively increase while advancing through the cortical hierarchy, supporting integration of
37 information (Chaudhuri et al., 2015; Murray et al., 2014). Whether a similar hierarchy of intrinsic
38 dynamics exists in the auditory system, and in particular within the temporal lobe, a hub for
39 auditory processing, remains underexplored.

40 In the auditory system, evidence for processing of external stimuli at multiple latencies stems
41 from studying evoked responses (Honey et al., 2012; Norman-Haignere et al., 2022). Primary
42 auditory areas show fast and short-lasting responses to sounds (Camalier et al., 2012).
43 Response latencies progressively increase while advancing in a processing hierarchy, from
44 primary to secondary areas, as for example the superior temporal gyrus (Nourski et al., 2014).
45 Beyond this 'classical' auditory cortex circuitry of the temporal lobe an extensive network of
46 adjacent cortical and deeper regions is also sensitive to auditory input and exhibits diverse
47 response profiles and latencies. At a cortical level, the insula for example shows relatively fast
48 auditory responses (Blenkman et al., 2019), while deeper structures, such as the hippocampus
49 and amygdala show slower, long-lasting responses to auditory stimuli (Halgren et al., 1980),
50 possibly mediating the integration of sensory information (Zuo et al., 2020).

51 This richness in auditory responses suggests that, when stimulated with sounds, the temporal
52 lobe facilitates auditory processing at multiple timescales (Stephens et al., 2013). These are
53 thought to reflect temporal “integration” windows that manifest in response to external stimuli
54 (Honey et al., 2012; Lerner et al., 2011; Norman-Haignere et al., 2022). Whether a similar
55 temporal lobe hierarchical organization also exists during rest and contributes to auditory
56 processing remains underexplored. Importantly, there is a critical lack of studies that
57 simultaneously assess neural timescales not only in the temporal cortex, but also in the
58 hippocampus and amygdala, which are key, yet underexplored regions in processing of auditory
59 information (Billig et al., 2022). The question of how these structures are positioned in a
60 hierarchy of intrinsic timescales remains therefore open. In humans, in particular, a fine-grained
61 measurement of neural dynamics in the temporal lobe can be challenging with non-invasive
62 techniques (Johnson et al., 2020; Raut et al., 2020; Tzovara et al., 2019), but evidence from
63 invasive recordings remains limited.

64 Here, we aimed at characterizing spontaneous intrinsic neural dynamics within cortical and
65 limbic structures of the extended auditory system, covering the temporal lobe and insula, and
66 their contribution to auditory processing. We focused on this network, which is relatively
67 accessible through intracranial electroencephalography (iEEG) recordings in patients with
68 pharmacoresistant epilepsies. We hypothesized that spontaneous intrinsic neural timescales,
69 estimated via the autocorrelation function (ACF) (Golesorkhi et al., 2021b; Zeraati et al., 2022),
70 or via the knee frequency of the power spectral density (PSD) (Gao et al., 2020) of iEEG
71 signals, would show a hierarchical organization within an extended auditory network, which
72 could, in turn, explain a hierarchy of neural responses to incoming auditory stimuli. We
73 additionally hypothesized that non-oscillatory brain dynamics, characterized by the spectral
74 exponent of aperiodic neural activity, which has been suggested to reflect a proxy of the

75 excitation to inhibition balance (Gao et al., 2017), would also reveal a hierarchical organization
76 across the temporal lobe.

77 Materials and Methods

78 Patients

79 We recorded intracranial EEG in 11 neurosurgical patients (4 women, median age=32 years,
80 min=27, max=56) with drug-refractory epilepsy who had been implanted with depth electrodes
81 to identify seizure foci (Table 1 for a detailed patient description). Electrode locations were
82 based on clinical criteria only. Recordings took place at the EPI Clinic, Zurich, and at the
83 Inselspital, Bern. The number of patients included in this study is following standards in the field
84 and is in line with, or larger than, existing intracranial studies investigating intrinsic neural
85 dynamics (Honey et al., 2012; Hullelt et al., 2016; Lendner et al., 2020; Mercier et al., 2022).
86 Patients provided written informed consent prior to participation in this research study, approved
87 by institutional ethics review boards of the Canton of Zurich (PB-2016-02055), and Inselspital,
88 Bern (# 2018-01387). All experiments were performed in accordance with the 6th Declaration of
89 Helsinki.

90 Experimental protocol

91 Patients were presented with auditory stimuli consisting of pure tones at three frequencies (500,
92 1250, 2500 Hz) with a random interstimulus interval between 0.9 and 19 seconds. Each tone
93 had a duration of 100 ms with 5 ms on/off ramps to avoid clicks. Interstimulus interval and tone
94 frequency were drawn from a pseudorandom distribution such that each was played 120 times
95 per hour (in total 360 tones per hour). Auditory stimuli were presented via in-ear headphones,
96 and their intensity was adjusted individually for each patient at a comfortable level. Patients
97 were instructed to relax and ignore the sounds. Some of the patients were additionally

98 presented with the auditory stimuli during sleep, at a later session, which was not analyzed in
99 the context of the present study.

100

101 iEEG recordings & preprocessing

102 Depth electrodes were used for iEEG recordings (DIXI Medical, 3 patients; Ad-Tech Medical, 8
103 patients) targeting different brain regions and varying from eight to eighteen platinum iEEG
104 contacts along their shaft. Data were recorded at 4096 or 1024 Hz. Recordings with 4096 Hz
105 sampling rate were downsampled offline to 1024 Hz.

106 All data were visually inspected to exclude electrodes with persistent spiking activity.
107 Continuous data were notch filtered around 50 Hz and harmonics, and re-referenced with a
108 bipolar scheme, i.e. each electrode to the closest one in the same electrode lead outwardly, to
109 remove any source of widespread noise. This was done to retain a local signal and mitigate
110 effects of volume conduction, following recommendations in the analysis of iEEG data (Lachaux
111 et al., 2012; Mercier et al., 2022). Peri-stimulus epochs were then extracted, spanning from -5 s
112 before the sounds' onset to 5 s post-stimulus onset. Only epochs that did not overlap with
113 another sound in this period were kept. All epochs were then visually inspected and any epochs
114 with remaining artifacts were rejected. The baseline period of each epoch was defined as the
115 interval [-1,0] s preceding the sounds. For studying auditory responses (see Responsive
116 electrodes section), the raw signal from all electrodes was additionally band-pass filtered
117 between 1-40 Hz. Processing of iEEG data was performed using MNE python (Gramfort et al.,
118 2013).

119 Electrode localization

120 Electrodes were localized on post-implant computed tomography (CT) scans using the Lead-
121 DBS toolbox (Horn & Kühn, 2015) and transformed into standard MNI coordinates for group

122 analyses. The post-implant CT scan was registered to a pre-implant structural T1-weighted
123 magnetic resonance imaging (MRI) scan from which anatomical labels were reconstructed using
124 the FreeSurfer toolbox and the Destrieux atlas. Subsequently, electrode coordinates identified
125 on the post-implant CT scans were mapped to their corresponding anatomical regions identified
126 on the pre-implant MRI. Anatomical label assignment was validated for all electrodes by an
127 expert neurologist, who verified their location and additionally ensured that none of the
128 electrodes that were included in our analyses were in white matter. The available electrodes
129 were divided across four regions of interest, covering the temporal cortex, the insula due to its
130 prominent auditory responses (included in temporal cortex), entorhinal cortex, hippocampus,
131 and amygdala. This resulted in N=270 electrodes in total, with a median=25, min=8 and max =
132 37 electrodes per patient (Table 1).

133 Intrinsic neural timescales

134 For estimating spontaneous intrinsic neural timescales, we first computed the Autocorrelation
135 function (ACF) on each epoch during 1 s baseline period (function *acf* from Python's
136 statsmodels (Seabold & Perktold, 2010)). The resulting ACFs across epochs were then
137 averaged to yield a single ACF for each electrode. We then defined the "intrinsic timescale" of
138 each electrode as the time lag at which the ACF reaches the value $1/e$, consistent with an
139 analytical decay of the form $f(t)=\exp(-t/\tau)$. The precise time-lag was computed by interpolating
140 with a spline fit to the ACF, as in (Raut et al., 2020).

141 To ensure that the estimation of timescales was not trivially driven by neural oscillations, we
142 performed two additional control analyses, following previous literature (Chaudhuri et al., 2015;
143 Gao et al., 2020; Murray et al., 2014; Zeraati et al., 2022). First, we fitted a curve of the form $f(t)$
144 $= a*\exp(-t/\tau) + (1-a)*\cos(2\pi ft)$ to the ACF with (a, τ, f) as parameters to be optimized (Zeraati et

145 al., 2022); a represents the amplitude parameter, f the putative oscillatory frequency, and τ the
146 estimated timescale. In a second control analysis, we computed timescales as the inverse of the
147 knee frequency in power spectra, estimated as $f_k = k^{1/exp}$ with k being the knee parameter and exp
148 the spectral exponent, as implemented in the `specparam` toolbox (Donoghue et al., 2020) in
149 “knee” mode. We fitted power spectra from 2 to 35 Hz, to have a reliable power estimate on the
150 lower limit and to keep consistency with the “fixed” spectral parametrization for the higher limit
151 (see next section for a discussion on the choice of frequency band). Electrodes where the
152 algorithm could not find a knee frequency were excluded.

153 Power spectral density and spectral exponent

154 For estimating the spectral exponent, we computed power spectra with a Hann-windowed and
155 detrended Fourier transform on the baseline period (function `spectrogram` from Python’s `scipy`
156 (Virtanen et al., 2020)). Power spectra were averaged using a “meanlog” approach, i.e. taking
157 the mean of the logarithm of the power spectra across epochs, to yield a single power spectrum
158 density for each electrode.

159 The spectral exponent was then computed on each electrode’s average power spectrum density
160 using the standard implementation of the spectral parameterization algorithm (Donoghue et al.,
161 2020) in the “fixed” mode (linear fit in log-log plot) in two different frequency ranges: a lower
162 one, at 20-35 Hz, and a higher one, at 80-150 Hz. The lower range was chosen following a
163 large body of literature in order to avoid low-frequency knees, high-power peaks and spectral
164 plateaus (Gerster et al., 2021), and has been previously linked with individual variations to
165 excitation to inhibition balance (Gao et al., 2017; Lendner et al., 2020). Different alternative, but
166 related, frequency ranges were tested in exploratory analyses on a subset of patients (for
167 example 30-45 Hz, or 20-40 Hz). All of those gave comparable results, and we used 20-35 Hz
168 for our analysis, as it was the band that more consistently avoided the above-mentioned

169 problems. The higher range was chosen as a typical high-frequency range that is often
170 computed in iEEG studies, as a proxy for neural firing (Lachaux et al., 2012). The spectral
171 exponent was computed as the slope of non-periodic parts of the power spectra observed at
172 each electrode via a standardized approach with the `specparam` toolbox (Donoghue et al.,
173 2020) (parameters for the fitting: *peak_threshold*=2, *min_peak_height*: 0.1, *peak_width_limits*:
174 [1, 10], with *max_n_peaks*=2 for the lower range and 0 for the higher one). Fits for every
175 electrode were visually inspected, and any electrodes with clear artifacts on the power spectra,
176 or where the fit was particularly noisy were excluded to ensure an accurate estimation of the
177 spectral exponent. After this step, all remaining electrodes (N= 270) had fits with R^2 of at least
178 0.8. Amygdalar electrodes from two patients had a prominent peak in their power spectra
179 around 40 Hz (Figure 5A), which was found for electrodes of the amygdala only, and not other
180 electrodes, and to the best of our knowledge was unrelated to any sources of noise, or
181 pathological findings in these patients. We confirmed that fitting of the spectral exponent was
182 not affected by these peaks in any of the two patients, which were outside the range of our fits.

183 Responsive electrodes

184 Responsive electrodes were identified following common approaches in the field of iEEG
185 (Dürschmid et al., 2016). Briefly, differences between the average signal in post-stimulus time
186 points $\bar{A}(t)$, and over the entire baseline \bar{B} , were compared with surrogate distributions
187 computed by randomly shifting the original epochs for $i=1, \dots, 1000$ iterations ($\{A_i(t)-B_i\}_{i=1 \dots 1000}$).
188 Response time points were considered significantly different from the baseline if $\bar{A}(t)-\bar{B}$ fell
189 outside the outer 5% interval of the permuted distribution. Additionally, only electrodes with at
190 least one consecutive response lasting more than 50 ms were kept, to correct for multiple
191 comparisons, as commonly done in the field (Guthrie & Buchwald, 1991; Haller et al., 2018;
192 Kam et al., 2021).

193 The post-stimulus time-points were restricted to the interval [10, 600] ms, to control for too early
194 and too late onsets that would be biologically implausible. We defined the onset latency as the
195 time between the sound onset and the first responsive timepoint, and the peak latency as the
196 time between the sound onset and the maximum absolute voltage difference from baseline.

197 Statistical analyses

198 Statistical tests were conducted in R version 4.2.0 (R Development Core Team, 2020) using
199 Linear Mixed-Effects models (LMEs) with a random intercepts term corresponding to the patient.
200 The random intercepts term captures inter-patient variability, which is needed when analyzing
201 electrodes from multiple patients together. This ensured that any identified effects were not
202 trivially driven by the fact that the electrodes were recorded from multiple patients (Yu et al.,
203 2022) (implemented with *nlme* package (Lindstrom & Bates, 1990)). The omnibus tests for the
204 “brain region” factor were computed with F-tests, while post-hoc pairwise comparisons were
205 computed with Tukey’s range test, controlling for multiple comparisons (implemented with
206 *emmeans* package). In the case of omnibus tests on multiple time lags (Fig. 2a) and tests over
207 multiple MNI coordinates, p-values were Bonferroni-corrected. For regression analyses, we
208 used LMEs with a continuous predictor and random intercepts accounting for across-patient
209 variability. We computed correlation values starting from R^2 as described in (Nakagawa &
210 Schielzeth, 2013) and took the square root, mimicking a fixed-effects-only linear model
211 (implemented with *MuMIn* package (Kamil Barton, 2020)). P-values were computed with F-tests,
212 correcting with Bonferroni when regressing on each level of the region factor separately (p_{corr}).

213 Data and code availability

214 Because of the sensitive nature of the data, data and code can be made available from the

215 corresponding author upon reasonable request.

216 Results

217 We analyzed iEEG signals in 270 electrodes from 11 epilepsy patients (median=25, min=8,
218 max=37 electrodes per patient, Table 1). In a first step, we assessed a macroscopic
219 organization of neural dynamics by dividing electrodes into four regions of interest, selected
220 based on the most consistent implantation schemes across patients. These were targeting the
221 entorhinal cortex (ENT), hippocampus (HIP), and amygdala (AMY) in their innermost electrodes,
222 and had additional electrodes covering the temporal and adjacent cortices (CTX) (Figure 1A for
223 an exemplar implantation). In a second step, we grouped all available electrodes together
224 (Figure 1B for full electrode coverage), irrespective of regions of interest, and assessed their
225 spatial organization at a finer level, with respect to cortical and limbic anatomies.

226 iEEG signals in the four regions of interest present striking qualitative differences already in their
227 ongoing neural activity prior to sound presentation (Figure 1B for exemplar iEEG recordings). To
228 characterize ongoing neural dynamics, we computed their intrinsic timescales prior to the
229 presentation of sounds (Figure 1A, middle). For each electrode, we computed the
230 autocorrelation function of baseline iEEG signals, which quantifies how similar a time series is to
231 its past values across multiple time-lags. The mean autocorrelation, computed across patients
232 and brain regions, shows a characteristic decay as the time lag increases (Figure 2A). For short
233 time lags, the mean autocorrelation follows an ordering: electrodes in the temporal cortex have
234 the most rapid decay, followed by electrodes in the entorhinal cortex, the hippocampus, and
235 last, the amygdala (Figure 2A), with significant differences across the four regions at time-lags
236 between 10 and 80 ms (mixed-effects models, accounting for different patients, $p_{\text{corr}} < 0.05$ with
237 Bonferroni correction) (Figure 2A, solid horizontal line).

238 We next computed intrinsic neural timescales (τ). These were defined as the time lag at which
239 the autocorrelation of each electrode decayed to a fixed value (in our case, $1/e$, Figure 2A,
240 dashed horizontal line). The extracted intrinsic timescales τ confirm the macroscopic hierarchy
241 observed via the autocorrelation function and show a significant difference across brain regions
242 ($F(3,256)=27.313$, $p=2.33\times 10^{-15}$, mixed-effects model with random intercepts) (Figure 2B). The
243 temporal cortex exhibits significantly faster intrinsic timescales, at 40.6 ms on average
244 compared to both the hippocampus and amygdala, which have slower timescales, at 56.1 and
245 63.3 ms, respectively (Table 2 for a detailed report of all paired statistical comparisons, based
246 on t-tests derived via the linear mixed effect models, and accounting for different patients).
247 Within subregions of the cortex, intrinsic timescales tend to be slower in the pole, and faster in
248 the transverse gyrus, while the superior, middle and inferior temporal cortex, and the insula lie in
249 between (Table 3). The entorhinal cortex (46.9 ms) is also significantly faster compared to other
250 limbic areas, but not different from the temporal cortex (Table 2).

251 These results were confirmed with two additional control analyses, which accounted for
252 potential biases due to oscillations. First, when estimating timescales by a direct exponential
253 decay fit to the ACFs, similar to (Murray et al., 2014; Siegle et al., 2021), but accounting for
254 oscillations (Zeraati et al., 2022), the same macroscopic hierarchy was observed, highlighted by
255 a significant difference of timescales across regions ($F(3,256)=16.789$, $p=5.49\times 10^{-10}$). Second,
256 the same hierarchy was also observed when estimating timescales as the inverse of the knee
257 frequency in power spectra, similar to (Gao et al., 2020), ($F(3,197)=28.769$, $p=1.78\times 10^{-15}$). Both
258 of these control analyses replicate the same ordering of timescales as reported in Figure 2B.
259 These findings reveal a robust macroscopic hierarchy in spontaneous neural activity, confirmed
260 with three different methods, where the temporal cortex shows short intrinsic timescales, while
261 limbic areas exhibit slower dynamics.

262 We then delved into a finer characterization of timescales by exploring their spatial organization
263 within anatomical regions (Table 3 for an overview of cortical subregions). Within the temporal
264 and entorhinal cortices, intrinsic timescales show a gradient that spans the temporal lobe
265 through the postero-lateral (fast timescales) to the antero-medial (slow timescales) axis,
266 following the temporal lobe anatomy (Figure 2C). This gradient is particularly prominent in the Y
267 and Z directions that mostly define the temporal lobe orientation (Figure 2D, correlation between
268 coordinates in MNI space and intrinsic timescales: $\rho_x=0.231$, $\rho_x=2.44\times 10^{-6}$; $\rho_y=0.292$,
269 $\rho_y=1.83\times 10^{-9}$; $\rho_z=-0.377$, $\rho_z=2.94\times 10^{-12}$, mixed-effects models and Bonferroni corrected).

270 The spatial distribution of timescales in the hippocampus and amygdala, on the contrary, is less
271 defined, with no significant correlation along any of the MNI coordinates after correcting for
272 multiple comparisons ($\rho_x=0.201$, $\rho_x=0.156$; $\rho_y=0.219$, $\rho_y=0.154$; $\rho_z=-0.159$, $\rho_z=0.443$, mixed-
273 effects models and Bonferroni corrected, Figure 3). These findings support a fine-grained
274 intrinsic organization of spontaneous neural dynamics in the extended auditory network, that
275 manifests across cortical and limbic regions, and exhibits an anatomical gradient spanning the
276 temporal cortex from posterior to anterior.

277 We next investigated whether intrinsic timescales at baseline could explain the timing of
278 auditory processing. At a qualitative level, auditory intracranial event-related potentials (iERPs)
279 show striking differences throughout the temporal lobe (Figure 4A). iERPs in primary auditory
280 regions (for example the transverse gyrus, Figure 4A, top row) show early, short-lasting, and
281 high-amplitude responses, while iERPs in the superior temporal gyrus have a later onset and
282 duration (Figure 4A, second row). By contrast, auditory responses in the hippocampus,
283 amygdala, and entorhinal cortex are smoother and long-lasting (Figure 4A, third to fifth rows),
284 similar to previous reports (Halgren et al., 1980).

285 To quantify these response profiles, we restricted our analysis to electrodes that showed a
286 significant 1-40 Hz iEEG response to the auditory stimuli compared to a pre-stimulus baseline
287 (*Methods, Responsive electrodes*, N=67 out of 270 total electrodes). For each responsive
288 electrode, we computed its response onset and peak latencies (Figure 4B). Cortical electrodes
289 show generally faster responses than hippocampal and amygdalar ones both for onset (30 ms
290 faster) and peak (50-60 ms faster). At the group level though, there is no significant effect of
291 brain region on onset latency ($F(3,55)=1.867$, $p=0.146$) and just barely on peak latency
292 ($F(3,55)=2.774$, $p=0.0499$, both mixed-effects models). In cortical subregions, the transverse
293 gyrus shows the earliest responses, followed by the superior temporal gyrus/sulcus, inferior and
294 middle temporal gyri (Table 3).

295 Interestingly, this variability in onset and peak latencies within and between brain regions can be
296 partially explained when accounting for differences in intrinsic timescales (Figure 4C). We
297 computed a regression of response latencies on intrinsic timescales, which shows a highly
298 significant main effect of timescale at baseline both on response onset ($\rho=0.353$, $p=0.0009$) and
299 peak latency ($\rho=0.409$, $p=0.0005$, both mixed-effects models with random intercepts, to account
300 for different patients). The strong regression of the onset of auditory responses on intrinsic
301 timescales at baseline holds for electrodes within the temporal cortex ($\rho=0.457$, $p_{\text{corr}}=0.0017$)
302 and hippocampus ($\rho=0.816$, $p_{\text{corr}}=0.0013$, Figure 4D) (mixed-effect models and Bonferroni
303 corrected). The other within-region regressions do not reach significance, except for the peak
304 latency in the hippocampus ($\rho_{\text{HIP}}=0.734$, $p_{\text{corr}}=0.031$). Moreover, a significant regression result
305 persists when splitting each patient's trials into two experimental halves, suggesting that the
306 observed results are robust across the experimental session ($\rho_1=0.429$, $p_1=0.001$; $\rho_2=0.364$,
307 $p_2=0.01$ for the first and second half of the experiment, respectively). These results show that
308 intrinsic timescales at baseline can explain both the onset and peak latencies of auditory
309 responses throughout the temporal lobe: regions that are characterized by fast intrinsic

310 timescales exhibit a fast reaction to incoming auditory stimuli, while the hippocampus,
311 amygdala, and entorhinal cortex are mediated by slower ongoing dynamics and show slower
312 auditory responses.

313 To further explore and confirm the observed hierarchy of intrinsic neural timescales, we
314 additionally characterized their aperiodic neural activity via the spectral exponent (Figure 5). The
315 average power spectral density shows qualitative differences across the four regions of interest
316 (Figure 5A). The cortex exhibits a characteristic oscillatory peak around 10 Hz, and a relatively
317 fast decay, while the hippocampus displays the strongest power, which for low frequencies
318 decays relatively gently, but after 70 Hz much faster (Figure 5A). We quantified the non-
319 oscillatory part of the power spectra for each electrode via the spectral exponent (i.e. the slope
320 in log-log space) in a lower (20-35 Hz, as commonly reported in the literature (Gao et al., 2017;
321 Lendner et al., 2020; Miskovic et al., 2019)) and upper range (80-150 Hz), corresponding to high
322 gamma power (Lachaux et al., 2012). The lower range was chosen after considering typical
323 ranges used in literature, which vary across studies, and compromising between consistency
324 with previous studies and recommended methodological considerations (see *Methods, Power*
325 *spectral density and spectral exponent* for a detailed explanation of the choice of the frequency
326 band and control analyses).

327 The spectral exponent in the 20-35 Hz range shows a strong ordering, with electrodes in the
328 temporal cortex having the steepest exponent, followed by electrodes in the entorhinal cortex,
329 hippocampus, and amygdala (Figure 5B), with a significant effect of region ($F(3,256)=80.665$,
330 $p=1.11\times 10^{-16}$). This result confirms the ordering observed for intrinsic timescales (Figure 2B),
331 with a different and complementary measure. Moreover, all pairs of cortical-limbic areas have
332 significant differences in their 20-35 Hz exponent (Table 4), while the difference between
333 temporal and entorhinal cortex is slightly below significance threshold (Table 4, $p_{\text{CTX-ENT}}=0.054$).
334 Exponents in cortical subregions do not show marked differences from each other (Table 3).

335 The spectral exponent in the 80-150 Hz range also shows a significant main effect of region
336 ($F(3,256)=79.156$, $p=1.11\times 10^{-16}$) (Figure 5C). This effect is mainly driven by the difference
337 between the hippocampus (with an exponent of 4.5 on average across electrodes) and all other
338 regions (Table 4), which instead have very similar exponent values, ranging between 2.4 and
339 2.6 on average (Figure 5C). The particularly steep hippocampal spectral exponent for high
340 frequencies reflects the abrupt change of slope in the power spectrum, which forms a knee at
341 around 70 Hz (Figure 5A).

342 As the lower range spectral exponent reflects the same ordering of brain regions as intrinsic
343 timescales, we explored its spatial organization. Similar to the intrinsic timescales, we observe
344 an anatomical modulation of spectral exponents along the temporal lobe, indicated by a
345 significant, albeit weaker, correlation between spectral exponent and MNI X coordinates ($\rho_x=-$
346 0.188 , $p_x=9.99\times 10^{-4}$, mixed-effects model and Bonferroni corrected), but no significant
347 correlation along other axes ($p>0.12$). This information provides further support for a gradient
348 organization of neural dynamics within the extended auditory cortical network.

349 Last, the spectral exponent within the hippocampus/amygdala only shows a weak correlation
350 along the X axis ($\rho_x=-0.252$, $p_x=0.029$, mixed-effects model and Bonferroni corrected). When
351 correlating the lower spectral exponent with response onset or peak latencies there is no
352 significant correlation, neither in all responsive electrodes grouped together ($\rho_{\text{onset}}=0.066$,
353 $p_{\text{onset}}=0.529$; $\rho_{\text{peak}}=-0.096$, $p_{\text{peak}}=0.430$, mixed-effects models) nor within any of the individual
354 brain regions (Table 5).

355 Discussion

356 We provide evidence for a hierarchy of spontaneous intrinsic neural dynamics in the extended
357 human auditory network, which in turn explains a hierarchy in the processing of incoming
358 auditory stimuli. At a macroscopic level, the temporal cortex assumes a “low” position along this
359 hierarchy, highlighted by a steep spectral exponent and short intrinsic timescales, which likely
360 mediate short temporal receptive windows (Honey et al., 2012; Norman-Haignere et al., 2022).
361 On the contrary, the hippocampus and amygdala exhibit longer intrinsic timescales and have
362 flatter spectral exponents. This suggests that the hippocampus and amygdala assume a
363 “higher”, or integrative, function in a temporal lobe hierarchy, as longer receptive time windows,
364 indicated by longer timescales, may be necessary for information integration (Golesorkhi et al.,
365 2021b; Murray et al., 2014). By contrast, a flatter exponent may indicate a shift towards
366 excitation (Gao et al., 2017), or increased neural noise (Alnes et al., 2021).

367 *Intrinsic timescales and spectral exponent reveal a hierarchy in the temporal lobe*

368 Our findings are in line with previous reports of a hierarchical organization in the visual and
369 somatosensory modalities (Murray et al., 2014; Wang, 2020), where neural timescales
370 progressively increase along the cortical hierarchy. Previous investigations of intrinsic
371 timescales in humans have mainly relied on hemodynamic and magnetoencephalographic
372 measures, and have shown fast spontaneous dynamics in the temporal lobe compared to
373 higher-level areas, like the prefrontal cortex, albeit only at a macroscopic level (Golesorkhi et al.,
374 2021a; Raut et al., 2020). Apart from timescales, oscillatory power and the spectral exponent
375 also show an intrinsic organization (Frauscher et al., 2018; Mahjoory et al., 2020). iEEG
376 oscillatory peaks transition from faster to slower frequencies along the posterior-to-anterior
377 temporal cortex (Frauscher et al., 2018), while primary auditory regions show weaker alpha and

378 stronger high-gamma power in their baseline activity compared to secondary auditory areas
379 (Billig et al., 2019). Here, we refine these observations by exploring the hierarchy of intrinsic
380 timescales within the extended auditory network of the temporal lobe.

381 From a signal processing perspective, timescales quantify the autocorrelation decay of neural
382 signals, while the spectral exponent measures the power decay of aperiodic neural activity
383 (Hasson et al., 2015; He et al., 2010). A steeper exponent may reflect decreased higher-
384 frequency activity, a rotation in the power spectra (Podvalny et al., 2015), or lower levels of
385 neural noise (Alnes et al., 2021; Voytek et al., 2015). As several mechanisms can explain
386 changes in the steepness of power spectra, associating those to neural timescales is neither
387 trivial nor unambiguous. At a physiological level, timescales are considered an indicator of a
388 neural system's memory capacity (Hasson et al., 2015), while the steepness of the spectral
389 exponent around the lower range we studied here is considered a proxy of excitation-to-
390 inhibition balance (Gao et al., 2017).

391 Importantly, similar to timescales, synaptic excitation and inhibition also manifest hierarchically:
392 while advancing through the visual hierarchy, excitatory connections increase, myelin content
393 decreases, and the expression of genes involved in synaptic transmission increases (Wang,
394 2020). In our data, the 20-35 Hz spectral exponent was steeper in the temporal cortex than in
395 the hippocampus or amygdala, similar to previous reports (Frauscher et al., 2018), and possibly
396 reflecting higher levels of inhibition, compatible with previous reports of increased inhibition in
397 sensory regions (Wang, 2020).

398 In our results, the macroscopic ordering that we identify via timescales is mirrored by the
399 spectral exponent and reflects the neurobiological proximity that one would expect between the
400 temporal/entorhinal cortex and hippocampus, which are all characterized by a laminar
401 organization of pyramidal neurons, as opposed to the amygdala whose basolateral nucleus

402 consists primarily of pyramidal cells without preferential orientation, and with a much higher
403 neural density (Dumas et al., 2011).

404 Overall, our findings support the notion that properties of neural dynamics are intrinsic (Wainio-
405 Theberge et al., 2022); to this, we add that they are also local in nature. Taking advantage of
406 the fine spatial resolution of intracranial recordings in humans, we show that a hierarchy of
407 intrinsic neural dynamics of the extended auditory network manifests as a continuous gradient
408 along the postero-lateral to antero-medial axis, following the anatomy of the temporal lobe, both
409 for intrinsic timescales and spectral exponent.

410 *Extending the hierarchy of intrinsic timescales to hippocampus and amygdala*

411 Importantly, contrary to the vast majority of existing studies (Gao et al., 2020; Honey et al.,
412 2012; Murray et al., 2014; Norman-Haignere et al., 2022), we extend the characterization of
413 intrinsic neural dynamics beyond cortical electrodes by including limbic structures, such as the
414 hippocampus and the amygdala. Previous studies have shown that prefrontal or parietal regions
415 assume the role of “higher-order” areas (Honey et al., 2012; Rocchi et al., 2021). Here, we
416 expand these well-studied hierarchies by showing that the hippocampus and amygdala can also
417 be positioned in a “higher” order compared to sensory areas, both in terms of intrinsic dynamics
418 (slower timescales and flatter exponent) and auditory response latencies.

419 To date, only few studies have attempted to characterize intrinsic timescales in the human
420 hippocampus and amygdala. These report intermixed results, with one magnetic resonance
421 imaging study showing gradients of timescales in the hippocampus in the range of few seconds
422 (Raut et al., 2020), and a study of neural firing reporting no differences in timescales between
423 the two structures (Hagemann et al., 2022). In our work, we also didn't find evidence for
424 gradients of timescales within the hippocampus and amygdala. There are several possible
425 explanations for these diverging results across studies, including the different overall temporal

426 sensitivity of the recorded signals, ranging from seconds to milliseconds, the electrode
427 coverage, or, in the case of hemodynamic responses, signal dropout (Raut et al., 2020), which
428 all together make the comparison of timescales extracted from different recording modalities
429 non-trivial (Manea et al., 2022).

430 Additionally, the extended auditory network includes the “what” and “where” pathways,
431 comprising prefrontal and parietal areas (Rauschecker & Scott, 2009). The “what”, or rostral,
432 pathway typically shows sustained responses and longer response latencies than the “where”,
433 or caudal, pathway (Jasmin et al., 2019). This dissociation can be observed in non-human and
434 human primates (Camalier et al., 2012; Hamilton et al., 2018; Scott et al., 2011). The lack of
435 frontal or parietal electrode coverage in our patient cohort didn’t allow investigating how
436 timescales are organized along the full extent of these pathways and how they would be
437 positioned relative to hippocampus/amygdala in a putative hierarchy. Future investigations could
438 expand beyond the temporal lobe, allowing a direct comparison of intrinsic timescales in limbic
439 structures and frontal or parietal cortex.

440 *Linking spontaneous intrinsic timescales and auditory processing*

441 Although several studies have posited that short intrinsic timescales may mediate fast
442 responses to incoming stimuli, we now provide direct evidence for the auditory system. Previous
443 studies have either analyzed intrinsic timescales in the auditory system while assessing whole-
444 brain dynamics (Gao et al., 2020; Golesorkhi et al., 2021a; Raut et al., 2020), without the
445 specificity of our work for the auditory system, or have investigated intrinsic timescales during
446 complex auditory stimuli like speech, as they unfold over time (Honey et al., 2012; Norman-
447 Haignere et al., 2022). Here, we show, for the first time, specifically for the extended auditory
448 system, that a hierarchical organization in spontaneous neural activity is strongly related to the
449 timing of processing short, evoked auditory stimuli.

450 Importantly, we show, in the same patients and recordings, that the diversity of intrinsic
451 timescales partially explains the richness of auditory responses that are observed in temporal
452 areas in terms of onset and peak latencies, at the single electrode level, with high spatial
453 resolution. Although our analyses are correlational, we posit that this repertoire of spontaneous
454 intrinsic timescales may support the auditory process itself, providing a variety of processing
455 windows (Golesorkhi et al., 2021b) both at a macroscopic level across brain regions, and also at
456 the millimeter level, following the anatomical organization of the temporal cortex. Here, we used
457 pure tones as a simple experimental model of auditory processing. Future studies can examine
458 how the characteristics of auditory stimuli, for example, their frequency or complexity, affect the
459 interplay between spontaneous and evoked activity, and whether trial-by-trial changes in
460 timescales may affect auditory processing and perception of individual sounds.

461 Last, although the spectral exponent mirrors the macroscopic hierarchy observed via intrinsic
462 timescales, in our data there was no direct link to the timing of auditory responses. Although the
463 spectral exponent is sensitive to auditory processing (Gyurkovics et al., 2022), or levels of
464 attention (Waschke et al., 2021), it doesn't seem to directly relate to their timing. We speculate
465 that the exponent may capture frequency-specific modulations in neural activity, rather than the
466 response latency itself, which may be better explained by the temporal "memory" of a signal.

467 *Conclusions*

468 Our results show a hierarchy of neural dynamics in the extended human auditory network that
469 manifests across cortical and limbic structures, exhibits anatomical gradients with millimeter
470 resolution, and can explain the temporal richness of neural responses to auditory stimuli.

471 References

- 472 Alnes, S. L., Lucia, M. D., Rossetti, A. O., & Tzovara, A. (2021). Complementary roles of neural
473 synchrony and complexity for indexing consciousness and chances of surviving in acute
474 coma. *NeuroImage*, *245*, 118638. <https://doi.org/10.1016/j.neuroimage.2021.118638>
- 475 Billig, A. J., Herrmann, B., Rhone, A. E., Gander, P. E., Nourski, K. V., Snoad, B. F., Kovach, C.
476 K., Kawasaki, H., Howard, M. A., & Johnsrude, I. S. (2019). A Sound-Sensitive Source of
477 Alpha Oscillations in Human Non-Primary Auditory Cortex. *Journal of Neuroscience*,
478 *39*(44), 8679–8689. <https://doi.org/10.1523/JNEUROSCI.0696-19.2019>
- 479 Billig, A. J., Lad, M., Sedley, W., & Griffiths, T. D. (2022). The hearing hippocampus. *Progress in*
480 *Neurobiology*, *218*, 102326. <https://doi.org/10.1016/j.pneurobio.2022.102326>
- 481 Blenkmann, A. O., Collavini, S., Lubell, J., Llorens, A., Funderud, I., Ivanovic, J., Larsson, P. G.,
482 Meling, T. R., Bekinschtein, T., Kochen, S., Endestad, T., Knight, R. T., & Solbakk, A.-K.
483 (2019). Auditory deviance detection in the human insula: An intracranial EEG study.
484 *Cortex*, *121*, 189–200. <https://doi.org/10.1016/j.cortex.2019.09.002>
- 485 Camalier, C. R., D'Angelo, W. R., Sterbing-D'Angelo, S. J., de la Mothe, L. A., & Hackett, T. A.
486 (2012). Neural latencies across auditory cortex of macaque support a dorsal stream
487 supramodal timing advantage in primates. *Proceedings of the National Academy of*
488 *Sciences*, *109*(44), 18168–18173. <https://doi.org/10.1073/pnas.1206387109>
- 489 Chaudhuri, R., Knoblauch, K., Gariel, M.-A., Kennedy, H., & Wang, X.-J. (2015). A Large-Scale
490 Circuit Mechanism for Hierarchical Dynamical Processing in the Primate Cortex. *Neuron*,
491 *88*(2), 419–431. <https://doi.org/10.1016/j.neuron.2015.09.008>
- 492 Donoghue, T., Haller, M., Peterson, E. J., Varma, P., Sebastian, P., Gao, R., Noto, T., Lara, A.
493 H., Wallis, J. D., Knight, R. T., Shestyuk, A., & Voytek, B. (2020). Parameterizing neural
494 power spectra into periodic and aperiodic components. *Nature Neuroscience*, *23*(12),

- 495 1655–1665. <https://doi.org/10.1038/s41593-020-00744-x>
- 496 Dumas, T., Attal, Y., Dubal, S., Jouvent, R., & George, N. (2011). Detection of activity from the
497 amygdala with magnetoencephalography. *IRBM*, *32*(1), 42–47.
498 <https://doi.org/10.1016/j.irbm.2010.11.001>
- 499 Dürschmid, S., Edwards, E., Reichert, C., Dewar, C., Hinrichs, H., Heinze, H.-J., Kirsch, H. E.,
500 Dalal, S. S., Deouell, L. Y., & Knight, R. T. (2016). Hierarchy of prediction errors for
501 auditory events in human temporal and frontal cortex. *Proceedings of the National*
502 *Academy of Sciences*, *113*(24), 6755–6760. <https://doi.org/10.1073/pnas.1525030113>
- 503 Frauscher, B., von Ellenrieder, N., Zemann, R., Doležalová, I., Minotti, L., Olivier, A., Hall, J.,
504 Hoffmann, D., Nguyen, D. K., Kahane, P., Dubeau, F., & Gotman, J. (2018). Atlas of the
505 normal intracranial electroencephalogram: Neurophysiological awake activity in different
506 cortical areas. *Brain*, *141*(4), 1130–1144. <https://doi.org/10.1093/brain/awy035>
- 507 Gao, R., Peterson, E. J., & Voytek, B. (2017). Inferring synaptic excitation/inhibition balance
508 from field potentials. *NeuroImage*, *158*, 70–78.
509 <https://doi.org/10.1016/j.neuroimage.2017.06.078>
- 510 Gao, R., van den Brink, R. L., Pfeffer, T., & Voytek, B. (2020). Neuronal timescales are
511 functionally dynamic and shaped by cortical microarchitecture. *ELife*, *9*, e61277.
512 <https://doi.org/10.7554/eLife.61277>
- 513 Gerster, M., Waterstraat, G., Litvak, V., Lehnertz, K., Schnitzler, A., Florin, E., Curio, G., &
514 Nikulin, V. (2021). *Separating neural oscillations from aperiodic 1/f activity: Challenges*
515 *and recommendations* (p. 2021.10.15.464483).
516 <https://doi.org/10.1101/2021.10.15.464483>
- 517 Golesorkhi, M., Gomez-Pilar, J., Tumati, S., Fraser, M., & Northoff, G. (2021a). Temporal
518 hierarchy of intrinsic neural timescales converges with spatial core-periphery
519 organization. *Communications Biology*, *4*(1), Article 1. [https://doi.org/10.1038/s42003-](https://doi.org/10.1038/s42003-021-01785-z)
520 [021-01785-z](https://doi.org/10.1038/s42003-021-01785-z)

- 521 Golesorkhi, M., Gomez-Pilar, J., Zilio, F., Berberian, N., Wolff, A., Yagoub, M. C. E., & Northoff,
522 G. (2021b). The brain and its time: Intrinsic neural timescales are key for input
523 processing. *Communications Biology*, 4(1), Article 1. [https://doi.org/10.1038/s42003-](https://doi.org/10.1038/s42003-021-02483-6)
524 021-02483-6
- 525 Gramfort, A., Luessi, M., Larson, E., Engemann, D., Strohmeier, D., Brodbeck, C., Goj, R., Jas,
526 M., Brooks, T., Parkkonen, L., & Hämäläinen, M. (2013). MEG and EEG data analysis
527 with MNE-Python. *Frontiers in Neuroscience*, 7.
528 <https://www.frontiersin.org/articles/10.3389/fnins.2013.00267>
- 529 Guthrie, D., & Buchwald, J. S. (1991). Significance Testing of Difference Potentials.
530 *Psychophysiology*, 28(2), 240–244. <https://doi.org/10.1111/j.1469-8986.1991.tb00417.x>
- 531 Gyurkovics, M., Clements, G. M., Low, K. A., Fabiani, M., & Gratton, G. (2022). Stimulus-
532 Induced Changes in 1/f-like Background Activity in EEG. *Journal of Neuroscience*,
533 42(37), 7144–7151. <https://doi.org/10.1523/JNEUROSCI.0414-22.2022>
- 534 Hagemann, A., Kehl, M. S., Dehning, J., Spitzner, F. P., Niediek, J., Wibral, M., Mormann, F., &
535 Priesemann, V. (2022). *Intrinsic timescales of spiking activity in humans during*
536 *wakefulness and sleep* (arXiv:2205.10308). arXiv.
537 <https://doi.org/10.48550/arXiv.2205.10308>
- 538 Halgren, E., Squires, N. K., Wilson, C. L., Rohrbaugh, J. W., Babb, T. L., & Crandall, P. H.
539 (1980). Endogenous Potentials Generated in the Human Hippocampal Formation and
540 Amygdala by Infrequent Events. *Science*, 210(4471), 803–805.
541 <https://doi.org/10.1126/science.7434000>
- 542 Haller, M., Case, J., Crone, N. E., Chang, E. F., King-Stephens, D., Laxer, K. D., Weber, P. B.,
543 Parvizi, J., Knight, R. T., & Shestyuk, A. Y. (2018). Persistent neuronal activity in human
544 prefrontal cortex links perception and action. *Nature Human Behaviour*, 2(1), Article 1.
545 <https://doi.org/10.1038/s41562-017-0267-2>
- 546 Hamilton, L. S., Edwards, E., & Chang, E. F. (2018). A Spatial Map of Onset and Sustained

- 547 Responses to Speech in the Human Superior Temporal Gyrus. *Current Biology*, 28(12),
548 1860-1871.e4. <https://doi.org/10.1016/j.cub.2018.04.033>
- 549 Hasson, U., Chen, J., & Honey, C. J. (2015). Hierarchical process memory: Memory as an
550 integral component of information processing. *Trends in Cognitive Sciences*, 19(6), 304–
551 313. <https://doi.org/10.1016/j.tics.2015.04.006>
- 552 Hasson, U., Yang, E., Vallines, I., Heeger, D. J., & Rubin, N. (2008). A Hierarchy of Temporal
553 Receptive Windows in Human Cortex. *Journal of Neuroscience*, 28(10), 2539–2550.
554 <https://doi.org/10.1523/JNEUROSCI.5487-07.2008>
- 555 He, B. J., Zempel, J. M., Snyder, A. Z., & Raichle, M. E. (2010). The Temporal Structures and
556 Functional Significance of Scale-free Brain Activity. *Neuron*, 66(3), 353–369.
557 <https://doi.org/10.1016/j.neuron.2010.04.020>
- 558 Honey, C. J., Thesen, T., Donner, T. H., Silbert, L. J., Carlson, C. E., Devinsky, O., Doyle, W.
559 K., Rubin, N., Heeger, D. J., & Hasson, U. (2012). Slow Cortical Dynamics and the
560 Accumulation of Information over Long Timescales. *Neuron*, 76(2), 423–434.
561 <https://doi.org/10.1016/j.neuron.2012.08.011>
- 562 Horn, A., & Kühn, A. A. (2015). Lead-DBS: A toolbox for deep brain stimulation electrode
563 localizations and visualizations. *NeuroImage*, 107, 127–135.
564 <https://doi.org/10.1016/j.neuroimage.2014.12.002>
- 565 Hullett, P. W., Hamilton, L. S., Mesgarani, N., Schreiner, C. E., & Chang, E. F. (2016). Human
566 Superior Temporal Gyrus Organization of Spectrotemporal Modulation Tuning Derived
567 from Speech Stimuli. *Journal of Neuroscience*, 36(6), 2014–2026.
568 <https://doi.org/10.1523/JNEUROSCI.1779-15.2016>
- 569 Jasmin, K., Lima, C. F., & Scott, S. K. (2019). Understanding rostral–caudal auditory cortex
570 contributions to auditory perception. *Nature Reviews Neuroscience*, 20(7), Article 7.
571 <https://doi.org/10.1038/s41583-019-0160-2>
- 572 Johnson, E. L., Kam, J. W. Y., Tzovara, A., & Knight, R. T. (2020). Insights into human cognition

- 573 from intracranial EEG: A review of audition, memory, internal cognition, and causality.
574 *Journal of Neural Engineering*, 17(5), 051001. <https://doi.org/10.1088/1741-2552/abb7a5>
- 575 Kam, J. W. Y., Helfrich, R. F., Solbakk, A.-K., Endestad, T., Larsson, P. G., Lin, J. J., & Knight,
576 R. T. (2021). Top-Down Attentional Modulation in Human Frontal Cortex: Differential
577 Engagement during External and Internal Attention. *Cerebral Cortex*, 31(2), 873–883.
578 <https://doi.org/10.1093/cercor/bhaa262>
- 579 Kamil Barton. (2020). *Mu-MIn: Multi-model inference, version 0.12.2/R18*. R Package Version.
580 <http://R-Forge.R-project.org/projects/mumin/>
- 581 Lachaux, J.-P., Axmacher, N., Mormann, F., Halgren, E., & Crone, N. E. (2012). High-frequency
582 neural activity and human cognition: Past, present and possible future of intracranial
583 EEG research. *Progress in Neurobiology*, 98(3), 279–301.
584 <https://doi.org/10.1016/j.pneurobio.2012.06.008>
- 585 Lendner, J. D., Helfrich, R. F., Mander, B. A., Romundstad, L., Lin, J. J., Walker, M. P., Larsson,
586 P. G., & Knight, R. T. (2020). An electrophysiological marker of arousal level in humans.
587 *ELife*, 9, e55092. <https://doi.org/10.7554/eLife.55092>
- 588 Lerner, Y., Honey, C. J., Silbert, L. J., & Hasson, U. (2011). Topographic Mapping of a
589 Hierarchy of Temporal Receptive Windows Using a Narrated Story. *Journal of*
590 *Neuroscience*, 31(8), 2906–2915. <https://doi.org/10.1523/JNEUROSCI.3684-10.2011>
- 591 Lindstrom, M. J., & Bates, D. M. (1990). Nonlinear Mixed Effects Models for Repeated
592 Measures Data. *Biometrics*, 46(3), 673–687. <https://doi.org/10.2307/2532087>
- 593 Mahjoory, K., Schoffelen, J.-M., Keitel, A., & Gross, J. (2020). The frequency gradient of human
594 resting-state brain oscillations follows cortical hierarchies. *ELife*, 9, e53715.
595 <https://doi.org/10.7554/eLife.53715>
- 596 Manea, A. M., Zilverstand, A., Ugurbil, K., Heilbronner, S. R., & Zimmermann, J. (2022). Intrinsic
597 timescales as an organizational principle of neural processing across the whole rhesus
598 macaque brain. *ELife*, 11, e75540. <https://doi.org/10.7554/eLife.75540>

- 599 Mercier, M. R., Dubarry, A.-S., Tadel, F., Avanzini, P., Axmacher, N., Cellier, D., Vecchio, M. D.,
600 Hamilton, L. S., Hermes, D., Kahana, M. J., Knight, R. T., Llorens, A., Megevand, P.,
601 Melloni, L., Miller, K. J., Piai, V., Puce, A., Ramsey, N. F., Schwiedrzik, C. M., ...
602 Oostenveld, R. (2022). Advances in human intracranial electroencephalography
603 research, guidelines and good practices. *NeuroImage*, *260*, 119438.
604 <https://doi.org/10.1016/j.neuroimage.2022.119438>
- 605 Miskovic, V., MacDonald, K. J., Rhodes, L. J., & Cote, K. A. (2019). Changes in EEG multiscale
606 entropy and power-law frequency scaling during the human sleep cycle. *Human Brain
607 Mapping*, *40*(2), 538–551. <https://doi.org/10.1002/hbm.24393>
- 608 Murray, J. D., Bernacchia, A., Freedman, D. J., Romo, R., Wallis, J. D., Cai, X., Padoa-
609 Schioppa, C., Pasternak, T., Seo, H., Lee, D., & Wang, X.-J. (2014). A hierarchy of
610 intrinsic timescales across primate cortex. *Nature Neuroscience*, *17*(12), Article 12.
611 <https://doi.org/10.1038/nn.3862>
- 612 Nakagawa, S., & Schielzeth, H. (2013). A general and simple method for obtaining R² from
613 generalized linear mixed-effects models. *Methods in Ecology and Evolution*, *4*(2), 133–
614 142. <https://doi.org/10.1111/j.2041-210x.2012.00261.x>
- 615 Norman-Haignere, S. V., Long, L. K., Devinsky, O., Doyle, W., Irobunda, I., Merricks, E. M.,
616 Feldstein, N. A., McKhann, G. M., Schevon, C. A., Flinker, A., & Mesgarani, N. (2022).
617 Multiscale temporal integration organizes hierarchical computation in human auditory
618 cortex. *Nature Human Behaviour*, *6*(3), Article 3. [https://doi.org/10.1038/s41562-021-
619 01261-y](https://doi.org/10.1038/s41562-021-01261-y)
- 620 Nourski, K. V., Steinschneider, M., McMurray, B., Kovach, C. K., Oya, H., Kawasaki, H., &
621 Howard, M. A. (2014). Functional organization of human auditory cortex: Investigation of
622 response latencies through direct recordings. *NeuroImage*, *101*, 598–609.
623 <https://doi.org/10.1016/j.neuroimage.2014.07.004>
- 624 Podvalny, E., Noy, N., Harel, M., Bickel, S., Chechik, G., Schroeder, C. E., Mehta, A. D.,

- 625 Tsodyks, M., & Malach, R. (2015). A unifying principle underlying the extracellular field
626 potential spectral responses in the human cortex. *Journal of Neurophysiology*, *114*(1),
627 505–519. <https://doi.org/10.1152/jn.00943.2014>
- 628 R Development Core Team. (2020). *R: A language and environment for statistical computing*. R
629 Foundation for Statistical Computing. <https://www.r-project.org/>
- 630 Rauschecker, J. P., & Scott, S. K. (2009). Maps and streams in the auditory cortex: Nonhuman
631 primates illuminate human speech processing. *Nature Neuroscience*, *12*(6), Article 6.
632 <https://doi.org/10.1038/nn.2331>
- 633 Raut, R. V., Snyder, A. Z., & Raichle, M. E. (2020). Hierarchical dynamics as a macroscopic
634 organizing principle of the human brain. *Proceedings of the National Academy of
635 Sciences*, *117*(34), 20890–20897. <https://doi.org/10.1073/pnas.2003383117>
- 636 Rocchi, F., Oya, H., Balezeau, F., Billig, A. J., Kocsis, Z., Jenison, R. L., Nourski, K. V., Kovach,
637 C. K., Steinschneider, M., Kikuchi, Y., Rhone, A. E., Dlouhy, B. J., Kawasaki, H.,
638 Adolphs, R., Greenlee, J. D. W., Griffiths, T. D., Howard, M. A., & Petkov, C. I. (2021).
639 Common fronto-temporal effective connectivity in humans and monkeys. *Neuron*,
640 *109*(5), 852-868.e8. <https://doi.org/10.1016/j.neuron.2020.12.026>
- 641 Scott, B. H., Malone, B. J., & Semple, M. N. (2011). Transformation of Temporal Processing
642 Across Auditory Cortex of Awake Macaques. *Journal of Neurophysiology*, *105*(2), 712–
643 730. <https://doi.org/10.1152/jn.01120.2009>
- 644 Seabold, S., & Perktold, J. (2010). Statsmodels: Econometric and Statistical Modeling with
645 Python. In S. van der Walt & J. Millman (Eds.), *Proceedings of the 9th Python in Science
646 Conference* (pp. 92–96). <https://doi.org/10.25080/Majora-92bf1922-011>
- 647 Siegle, J. H., Jia, X., Durand, S., Gale, S., Bennett, C., Graddis, N., Heller, G., Ramirez, T. K.,
648 Choi, H., Luviano, J. A., Groblewski, P. A., Ahmed, R., Arkhipov, A., Bernard, A., Billeh,
649 Y. N., Brown, D., Buice, M. A., Cain, N., Caldejon, S., ... Koch, C. (2021). Survey of
650 spiking in the mouse visual system reveals functional hierarchy. *Nature*, *592*(7852),

- 651 Article 7852. <https://doi.org/10.1038/s41586-020-03171-x>
- 652 Stephens, G. J., Honey, C. J., & Hasson, U. (2013). A place for time: The spatiotemporal
653 structure of neural dynamics during natural audition. *Journal of Neurophysiology*, *110*(9),
654 2019–2026. <https://doi.org/10.1152/jn.00268.2013>
- 655 Tzovara, A., Meyer, S. S., Bonaiuto, J. J., Abivardi, A., Dolan, R. J., Barnes, G. R., & Bach, D.
656 R. (2019). High-precision magnetoencephalography for reconstructing amygdalar and
657 hippocampal oscillations during prediction of safety and threat. *Human Brain Mapping*,
658 *40*(14), 4114–4129. <https://doi.org/10.1002/hbm.24689>
- 659 Vezoli, J., Vinck, M., Bosman, C. A., Bastos, A. M., Lewis, C. M., Kennedy, H., & Fries, P.
660 (2021). Brain rhythms define distinct interaction networks with differential dependence
661 on anatomy. *Neuron*, *109*(23), 3862–3878.e5.
662 <https://doi.org/10.1016/j.neuron.2021.09.052>
- 663 Virtanen, P., Gommers, R., Oliphant, T. E., Haberland, M., Reddy, T., Cournapeau, D.,
664 Burovski, E., Peterson, P., Weckesser, W., Bright, J., van der Walt, S. J., Brett, M.,
665 Wilson, J., Millman, K. J., Mayorov, N., Nelson, A. R. J., Jones, E., Kern, R., Larson, E.,
666 ... van Mulbregt, P. (2020). SciPy 1.0: Fundamental algorithms for scientific computing
667 in Python. *Nature Methods*, *17*(3), Article 3. <https://doi.org/10.1038/s41592-019-0686-2>
- 668 Voytek, B., Kramer, M. A., Case, J., Lepage, K. Q., Tempesta, Z. R., Knight, R. T., & Gazzaley,
669 A. (2015). Age-Related Changes in 1/f Neural Electrophysiological Noise. *Journal of*
670 *Neuroscience*, *35*(38), 13257–13265. <https://doi.org/10.1523/JNEUROSCI.2332-14.2015>
- 671 Wainio-Theberge, S., Wolff, A., Gomez-Pilar, J., Zhang, J., & Northoff, G. (2022). Variability and
672 task-responsiveness of electrophysiological dynamics: Scale-free stability and oscillatory
673 flexibility. *NeuroImage*, *256*, 119245. <https://doi.org/10.1016/j.neuroimage.2022.119245>
- 674 Wang, X.-J. (2020). Macroscopic gradients of synaptic excitation and inhibition in the neocortex.
675 *Nature Reviews Neuroscience*, *21*(3), Article 3. <https://doi.org/10.1038/s41583-020->
676 0262-x

- 677 Waschke, L., Donoghue, T., Fiedler, L., Smith, S., Garrett, D. D., Voytek, B., & Obleser, J.
678 (2021). *Modality-specific tracking of attention and sensory statistics in the human*
679 *electrophysiological spectral exponent* (p. 2021.01.13.426522).
680 <https://doi.org/10.1101/2021.01.13.426522>
- 681 Yu, Z., Guindani, M., Grieco, S. F., Chen, L., Holmes, T. C., & Xu, X. (2022). Beyond t test and
682 ANOVA: Applications of mixed-effects models for more rigorous statistical analysis in
683 neuroscience research. *Neuron*, *110*(1), 21–35.
684 <https://doi.org/10.1016/j.neuron.2021.10.030>
- 685 Zeraati, R., Shi, Y.-L., Steinmetz, N. A., Gieselmann, M. A., Thiele, A., Moore, T., Levina, A., &
686 Engel, T. A. (2022). *Intrinsic timescales in the visual cortex change with selective*
687 *attention and reflect spatial connectivity* (p. 2021.05.17.444537). bioRxiv.
688 <https://doi.org/10.1101/2021.05.17.444537>
- 689 Zuo, X., Honey, C. J., Barense, M. D., Crombie, D., Norman, K. A., Hasson, U., & Chen, J.
690 (2020). Temporal integration of narrative information in a hippocampal amnesic patient.
691 *NeuroImage*, *213*, 116658. <https://doi.org/10.1016/j.neuroimage.2020.116658>
692

693 **Table legends**

694 **Table 1.** Overview of patients dataset. We collected data from a total of 270 electrodes from 11
695 patients, with a median of 25 electrodes per patient and minimum and maximum of 8 and 37
696 electrodes. For each patient, we report gender, age, the hospital where the data were collected,
697 the number of electrodes used for our analyses, the hemisphere(s) where the electrodes were
698 implanted and the regions sampled from the retained electrodes.

699 **Table 2.** Pairwise comparisons of intrinsic neural timescales across regions of interest. The first
700 column lists each of the six pairwise comparisons, the second one the relative degrees of
701 freedom of the test, the third one the t-values of the post-hoc t-test, and the last column the
702 related p-values. All pairs of cortical-limbic areas have significant differences in their intrinsic
703 timescales, while the differences between temporal/entorhinal cortex and
704 hippocampus/amygdala are non-significant. The timescale values per region are computed
705 through a mixed-effects model with a patient-specific random effect and p-values are corrected
706 for multiple comparisons via the Tukey range test. D.O.F.: degrees of freedom.

707 **Table 3.** Intrinsic neural timescales, iERP latencies and the spectral exponent across cortical
708 subregions. The number of total and responsive electrodes across all recordings is reported for
709 each subregion, together with median values of timescales, auditory latencies, and 20-35 Hz
710 exponent. The fastest timescales and lower response latencies are observed for the transverse
711 temporal gyrus, while the opposite is true for the temporal pole. TTG: transverse temporal
712 gyrus, STG: superior temporal gyrus, STS: superior temporal sulcus, MTG: middle temporal
713 gyrus, ITG: inferior temporal gyrus, ITS: inferior temporal sulcus.

714 **Table 4.** Pairwise comparisons of spectral exponents among the four regions of interest in the
715 two analyzed frequency ranges (20-35 Hz and 80-150 Hz). The first column lists each of the six

716 pairwise comparisons, the second one the relative degrees of freedom of the test, the third and
717 fourth ones the t-values and p-values of the post-hoc t-test for the 20-35 Hz range, and the last
718 two columns the t-values and p-values for the 80-150 Hz range. All pairs of cortical-limbic areas
719 have significant differences in their 20-35 Hz exponent, while the difference between temporal
720 and entorhinal cortex is slightly below significance threshold. For the 80-150 Hz range, only the
721 comparisons between hippocampus and the other areas are significant due to the very steep
722 slope of hippocampal electrodes in the high-gamma range. The spectral exponent values are
723 computed through a mixed-effects model with a patient-specific random effect and p-values are
724 corrected for multiple comparisons via the Tukey range test. D.O.F.: degrees of freedom.

725 **Table 5.** Regressions of iERP auditory latencies on the 20-35 Hz spectral exponent at baseline.
726 The correlation coefficients and relative p-values are summarized when regressing onset and
727 peak iERP latencies on the spectral exponent, for all responsive electrodes. Regressions are
728 computed with mixed-effects models with a patient-specific random effect and p-values for the
729 four regions are Bonferroni corrected.

730 Figure legends

731 **Figure 1. Experimental paradigm, electrode coverage, and exemplar iEEG traces.** A.
732 Summary of the main analyses and methodology. Left: schematic of the auditory stimulation
733 protocol: Patients were presented with 100 ms pure tones, occurring at random intervals
734 between 0.9-19 s. Middle: Example of implanted iEEG electrodes and exemplar raw trace of
735 spontaneous neural activity from one electrode, before sound presentation, which is used to
736 estimate intrinsic timescales and spectral exponents. Right: intracranial event-related potentials
737 (iERPs) are extracted in response to the sounds. These are displayed for a schematic
738 illustration of our protocol, for three exemplar electrodes, presented in more detail in Figure 4. B.

739 Illustration of recorded electrodes (N=270) over the group of 11 patients. Black-circled
740 electrodes are responsive to the auditory stimulation. As exemplar signals, we show iEEG
741 traces from the transverse and superior temporal gyri (TTG and STG, pink), the entorhinal
742 cortex (light blue), the hippocampus (orange), and the amygdala (green). Each of these regions
743 exhibits characteristic and distinct spontaneous dynamics, displayed here over a 6 s segment.

744 **Figure 2. Autocorrelation function and intrinsic cortical neural timescales at baseline.** A.

745 Average autocorrelation function at baseline across electrodes and patients, for electrodes in
746 the temporal (pink) and entorhinal (light blue) cortices, hippocampus (orange), and amygdala
747 (green). The autocorrelation shows a significant main effect of region for time lags between 10
748 and 80 ms (horizontal solid bar). The dashed horizontal line at $1/e$ (inverse of natural logarithm)
749 displays the value of the autocorrelation for which the characteristic timescales are extracted. B.

750 Intrinsic timescales at baseline (τ), plotted for each electrode, show a main effect of region, with
751 significantly faster timescales for the temporal and entorhinal cortices compared to the
752 hippocampus and amygdala. C. The spatial organization of intrinsic timescales follows the
753 cortical anatomy. Electrodes in the posterior/superior temporal cortex exhibit the fastest
754 timescales, which progressively increase along the anterior/inferior axis. The color map
755 quantifies the intrinsic timescale for each electrode on a logarithmic scale. For display purposes,
756 all electrodes were projected to the left hemisphere. D. Gradients of timescales spanning the
757 cortex, plotted as timescales along the X, Y, and Z directions of MNI coordinates of each
758 electrode. Timescales significantly correlate with MNI coordinates in all three dimensions,
759 tracking the cortical anatomy.

760 **Figure 3. Intrinsic hippocampal and amygdalar neural timescales at baseline.** A.

761 Anatomical organization of intrinsic timescales at baseline throughout the hippocampus and
762 amygdala, displaying generally shorter timescales in hippocampus (darker colors) than in
763 amygdala, as in Figure 2B. The color map quantifies the intrinsic timescale for each electrode

764 on a logarithmic scale. For display purposes, all electrodes were projected to the left
765 hemisphere. B. Correlations between MNI coordinates and intrinsic timescale (τ) across
766 electrodes. Although τ tends to be slower for anterior electrodes, and in particular for the
767 amygdala, correlations in the X, Y, and Z directions are not significant when accounting for
768 different patients and after Bonferroni correction.

769

770 **Figure 4. Onset and peak latencies of auditory responses across brain regions and their**

771 **relation to intrinsic timescales at baseline.** A. Exemplar auditory responses for each of the

772 recorded regions (1-40 Hz iERPs). Time 0 corresponds to sound onset. Auditory responses in

773 the transverse temporal gyrus (TTG) are the earliest, shorter-lasting, and exhibit the largest

774 amplitude (top plot). Responses in other cortical regions, e.g. the superior temporal gyrus

775 (STG), have a relatively early onset, and later peak, while responses in the entorhinal cortex,

776 hippocampus, and amygdala (third to fifth row) are typically smoother, long-lasting, and with

777 later peaks. Significant response periods compared to the pre-stimulus baseline are highlighted

778 in blue. The variability in response amplitudes is indicated by the different spans of a $10\mu\text{V}$

779 scale on the y-axis. B. Auditory response onset (left panel) and peak (right panel) latencies for

780 all responsive electrodes. The temporal cortex shows the earliest onset and peak latencies

781 across all brain regions, with responses starting on average at 168.7 ms, and peaking at 259 ms

782 after sound onset, followed by the hippocampus/amygdala, and entorhinal cortex. C.

783 Regression of auditory iERP onset (y-axis, left panel) and peak (y-axis, right panel) latencies on

784 intrinsic timescales τ at baseline (x-axis) across all responsive electrodes. Regressions of both

785 onsets and peaks on intrinsic timescales are highly significant, accounting for across-patient

786 variations, suggesting that intrinsic timescales can explain the timing of auditory responses at

787 the single electrode level. D. A significant regression of iERP onsets on intrinsic timescales also

788 persists within the temporal cortex (left panel), and hippocampus only (right panel), but not in
789 the amygdala or entorhinal cortex.

790 **Figure 5. Power spectra and spectral exponents across brain regions.** A. Average power
791 spectra are displayed for the four regions of interest. Cortex (pink) exhibits a characteristic
792 oscillatory peak around 10 Hz, and a relatively fast decay, while the hippocampus (orange)
793 displays the strongest power, which for low frequencies decays relatively gently, but after 70 Hz
794 much faster. The shaded rectangles highlight the two frequency ranges for which the spectral
795 exponent is computed, at 20-35 Hz, and at 80-150 Hz. x- and y-axes are plotted in logarithmic
796 scales. B/C. Spectral exponent at 20-35 Hz (B) and 80-150 Hz (C), for each electrode and
797 region of interest. The spectral exponent in the 20-35 Hz range shows a significant main effect
798 of region, with the temporal cortex having the steepest exponent followed by the entorhinal
799 cortex, the hippocampus, and amygdala, which have flatter exponents. The spectral exponent at
800 80-150 Hz also shows a significant effect of region, with the hippocampus having the steepest
801 exponent among all other regions, compatible with the knee observed in the average power
802 spectra (panel A).

803 Tables

Patient ID	Gender	Age	Clinic	# of electrodes analyzed	Hemisphere	Regions
1	M	31	Zürich	25	L + R	CTX, ENT, HIP, AMY
2	F	33	Bern	17	R	CTX, ENT, HIP
3	F	29	Zürich	34	L + R	CTX, ENT, HIP, AMY
4	F	30	Zürich	30	L + R	CTX, ENT, HIP, AMY
5	M	56	Zürich	28	L + R	CTX, ENT, HIP, AMY
6	M	42	Zürich	20	L	CTX, ENT, HIP, AMY
7	M	34	Zürich	37	L + R	CTX, ENT, HIP, AMY
8	F	45	Bern	24	L	CTX, ENT, HIP
9	M	29	Zürich	28	L + R	CTX, ENT, HIP, AMY
10	M	27	Zürich	19	R	CTX, ENT, HIP, AMY

11	M	32	Bern	8	L	CTX, HIP
----	---	----	------	---	---	----------

804 Table 1

805

Comparison	D.O.F.	t-value	p-value
CTX-ENT	192	-2.383	0.083
CTX-HIP	198	-6.099	2.34×10^{-8}
CTX-AMY	184	-7.716	1.69×10^{-12}
ENT-HIP	82	-2.817	0.027
ENT-AMY	68	-4.635	3.36×10^{-5}
HIP-AMY	74	-2.067	0.167

806 Table 2

807

Cortical subregion	# electrodes (responsive)	Median timescale (ms)	Median iERP onset (ms)	Median iERP peak (ms)	Median exponent (a.u.)
TTG	3 (3)	16.7	42.0	80.1	2.1
STG + STS	54 (13)	31.2	83.0	168.9	3.4

MTG	18 (2)	30.0	189.0	293.5	3.5
ITG + ITS	19 (2)	32.1	133.8	286.6	3.4
Insula	22 (8)	31.3	131.3	276.9	2.7
Pole	13 (3)	41.4	260.7	438.5	3.9

808 Table 3

809

Comparison	D.O.F.	t-value (20-35 Hz)	p-value (20-35 Hz)	t-value (80-150 Hz)	p-value (80-150 Hz)
CTX-ENT	192	2.557	0.054	1.551	0.408
CTX-HIP	198	12.421	4.34×10^{-14}	-14.214	4.31×10^{-14}
CTX-AMY	184	11.409	5.35×10^{-14}	1.631	0.363
ENT-HIP	82	7.591	3.63×10^{-12}	-12.321	4.35×10^{-14}
ENT-AMY	68	7.564	4.27×10^{-12}	0.195	0.997
HIP-AMY	74	0.608	0.929	11.650	4.90×10^{-14}

810 Table 4

811

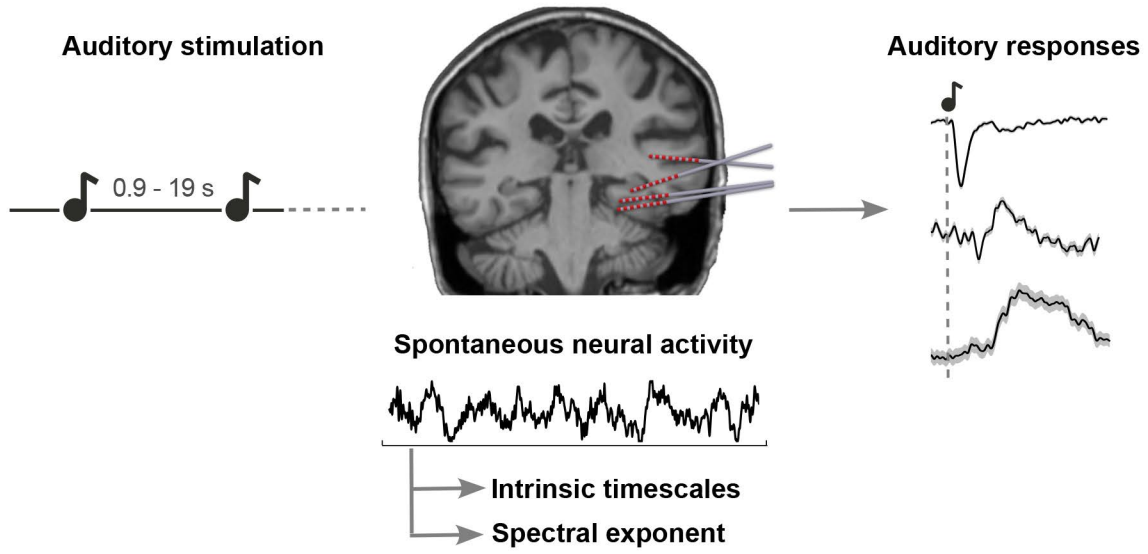
812

Region	Correlation ρ (iERP onset)	p-value (iERP onset)	Correlation ρ (iERP peak)	p-value (iERP peak)
All	0.066	0.53	-0.096	0.43
CTX	0.381	0.12	0.345	0.21
ENT	0.669	0.73	-0.276	1.0
HIP	0.313	1.0	0.215	1.0
AMY	-0.237	1.0	-0.340	0.93

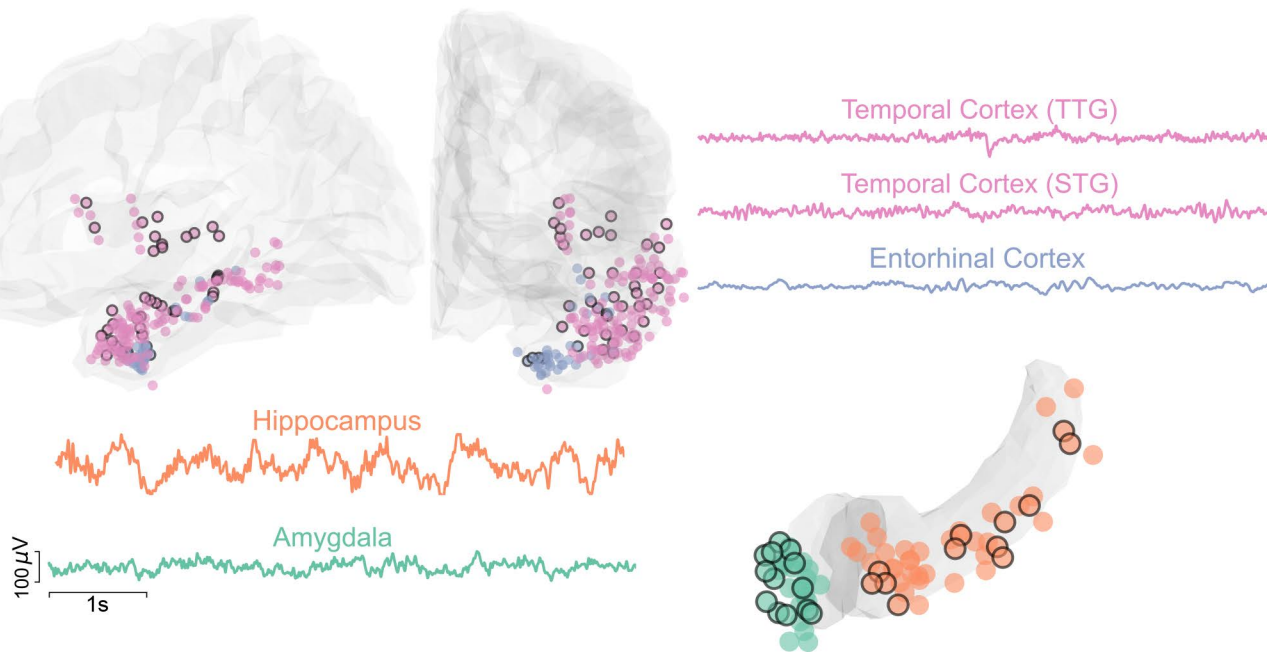
813 Table 5

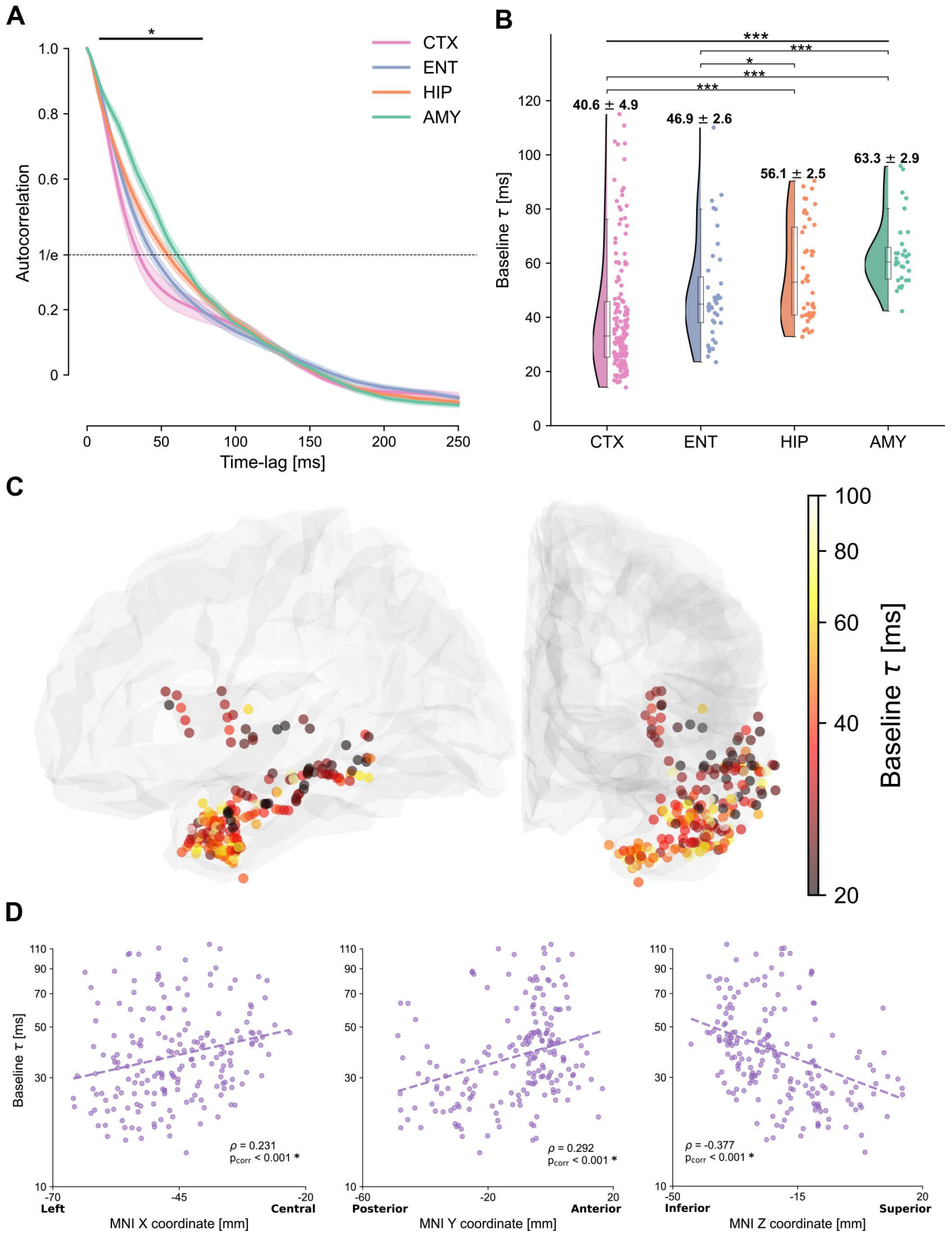
814

A

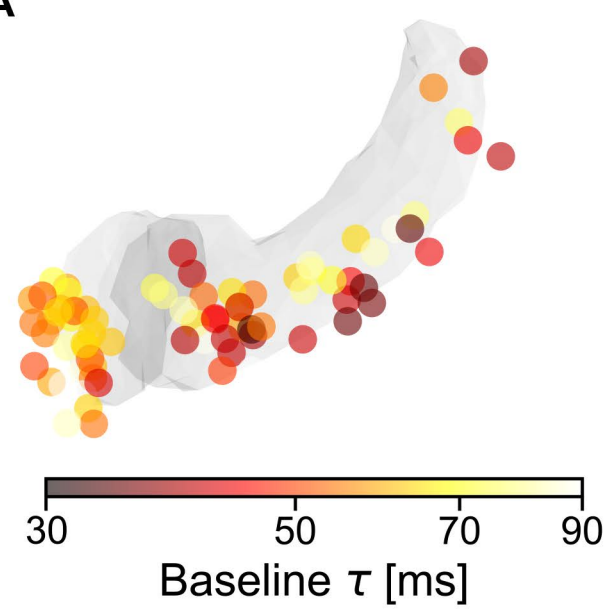


B





A



B

